RF METROLOGY OF LUNAR HIGHLANDS REGOLITH SIMULANT NU-LHT-2M

Ka and Broadband Communications Conference*, Bradford, UK, 23-26 October 2023*

Kerry J. Johnson, Elise M. Eckman, Aaron J. Swank, Michael J. Zemba
NASA Glenn Research Center, 21000 Brookpark Rd, Cleveland, OH

Regolith Characterization

Understanding the electrical properties of lunar regolith is vital to modeling radiofrequency (RF) propagation on the lunar surface.

Landing site regolith properties vary; partially due to impact events[1].

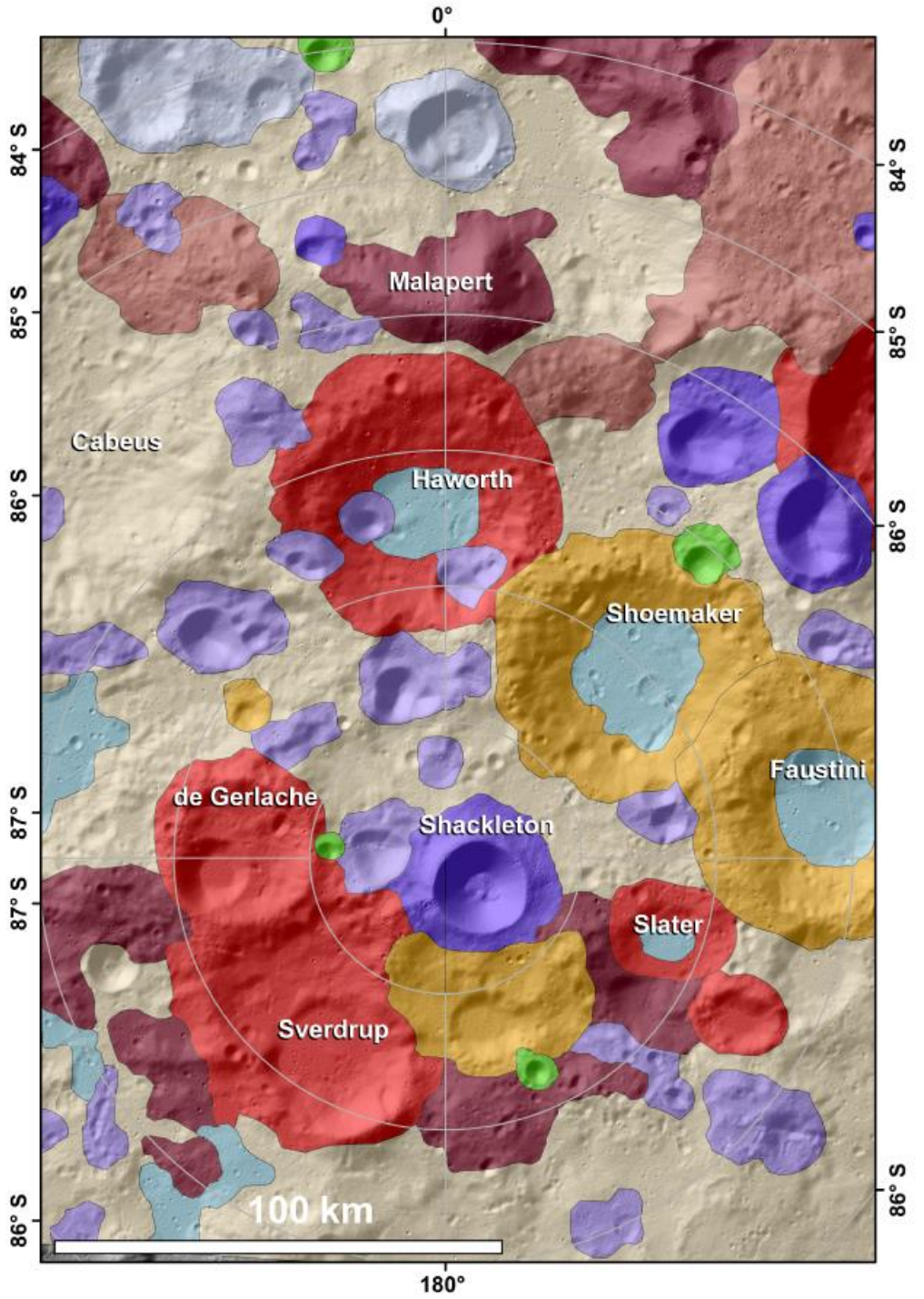

Geological Units of Spudis et al. (2008)

- Eratosthenian crater materials
- Imbrian crater materials
- Orientale basin secondary crater material
- Imbrium basin secondary crater material
- Imbrian plains materials
- Nectarian crater materials
- pre-Nectarian crater materials
- pre-Nectarian massif
- pre-Nectarian platform massif material
- pre-Nectarian terra material

1. *Spudis et al., "Geography of Shackleton Crater and the south pole of the Moon." Geophys. Res. Lett. 35, 2008.*
2. *Chunyu Ding et al., "Compositional variations along the route of Chang'e-3 Yutu rover recrealed by the lunar penetrating radar". Progress in Earth and Planetary Science, 2020.*
3. *Chunlai Li et al., "The Moon's farside shallow subsurface structure unveiled by Chan'e-4 Lunar Penetrating Radar". Science Advances, Vol. 6 No. 9, 2020.*
4. *Jialong Lai et al., "Comparison of Dielectric Properties and Structure of Lunar Regolith at Chang'e-3 and Chang'e-4 Landing Sites…". Geophysical Research Letters, 46, 2019.*
5. *H.E Bussey et al., "Dielectric Measurements of Lunar Soil". Lunar and Planetary Science Conference IX, 1978.*

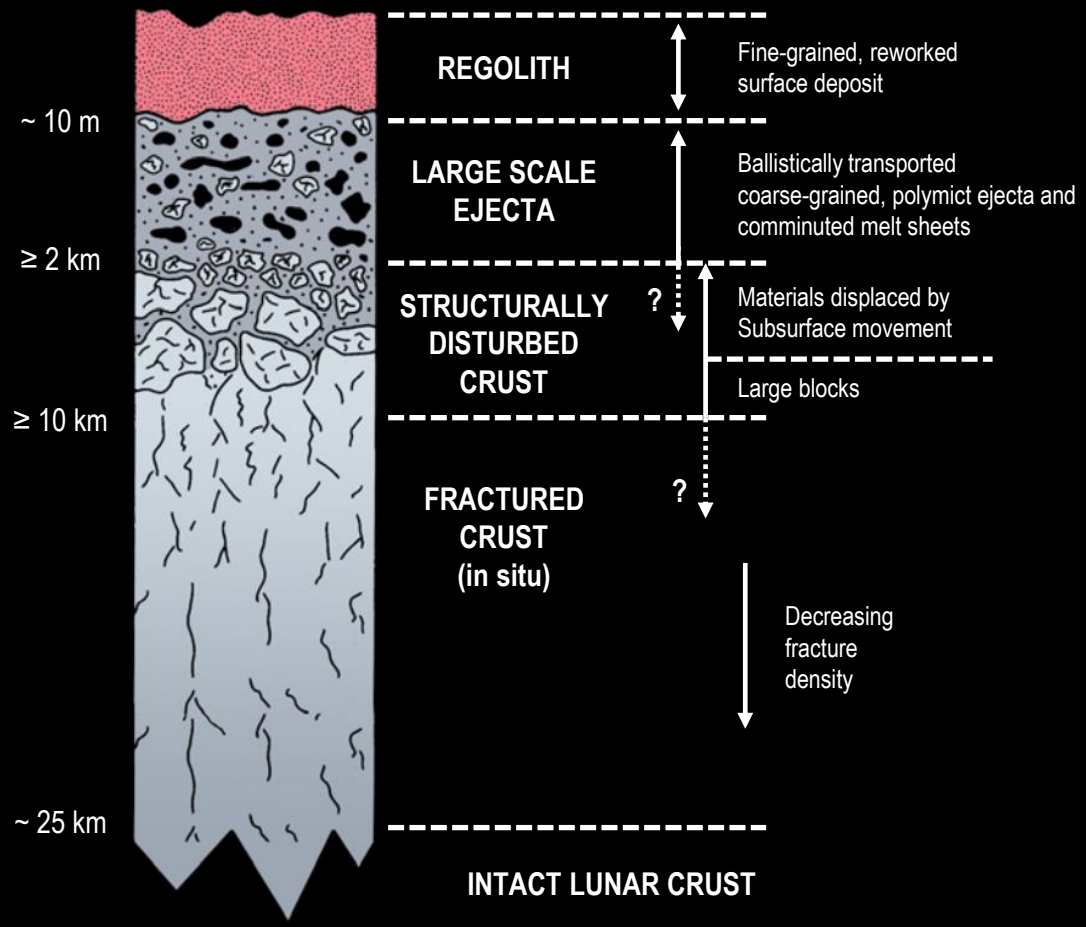

Site-to-site variation is expected and can significantly impact propagation models and system design. Variations in permittivity, loss tangent, depth, clutter (rocks/boulders) may be expected based on the unique geological history of each region. From the Connecting Ridge, a DTE link to Earth, which grazes Malapert Massif 125 km away, propagates across at least six distinct geological regions. [1]

Data from Chang'e-3 (near side, Mare Imbrium) and Chang'e-4 (far side, South Pole Aitken Basin) have demonstrated such variations in permittivity and regolith depth. [2]

Lofted and suspended clouds of charged regolith may also present challenges for the novel mission architectures of Artemis with numerous surface-to-surface and low elevation angle links.

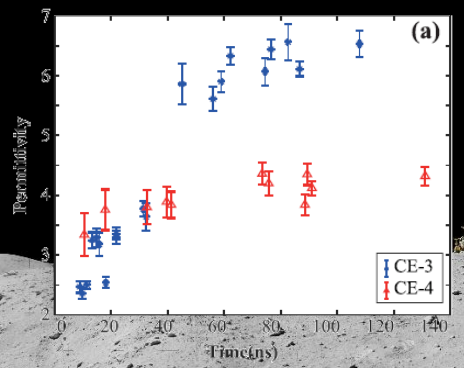

1. *Spudis et al., "Geography of Shackleton Crater and the south pole of the Moon." Geophys. Res. Lett. 35, 2008.*
2. *Liu, S., et al., "Pattern analyses of lunar penetrating radar images at Chang'E-3, 4, and 5 landing sites: A new insight into the evolution of lunar regolith". Journal of Geophysical Research: Planets, 128, June 2023.*

Frequency Ranges Tested with Lunar Simulants

Lunar Surface (Simulant tests)		LS to LO (Simulant tests)		LO to LS (Simulant tests)		LS to Earth (Simulant tests)		Earth to LS (Simulant tests)	
LunaNet Range	Tested Range	LunaNet Range	Tested Range	LunaNet Range	Tested Range	LunaNet Range	Tested Range	LunaNet Range	Tested Range
390-405MHz	0.4-20GHz	0.406-0.4061GHz	0.4-20GHz	2.025-2.110GHz	1.8-3.5GHz 0.4-20GHz 1-6GHz	8.45-8.5GHz	0.4-20GHz 8.2-12.4GHz	7.19-7.235GHz	7.2GHz 0.4-20GHz
435-450MHz	0.4-20GHz	2.2-2.29GHz	1.8-3.5GHz 1-6GHz 0.4-20GHz	23.15-23.55GHz		25.5-27GHz		22.55-23.15GHz	
2.4-2.48GHz	2.45GHz 2.47GHz 1.8-3.5GHz 0.4-20GHz 1-6GHz	27-27.5GHZ							
2.5035-2.62GHz	1.8-3.5GHz 0.4-20GHz 2.6-3.95GHz 1-6GHz 2.5GHz								
5.15-5.835GHz	0.4-20GHz 1-6GHz								
25.25-25.5GHz									
27.225-27.5GHz									

RF Data missing from key bands

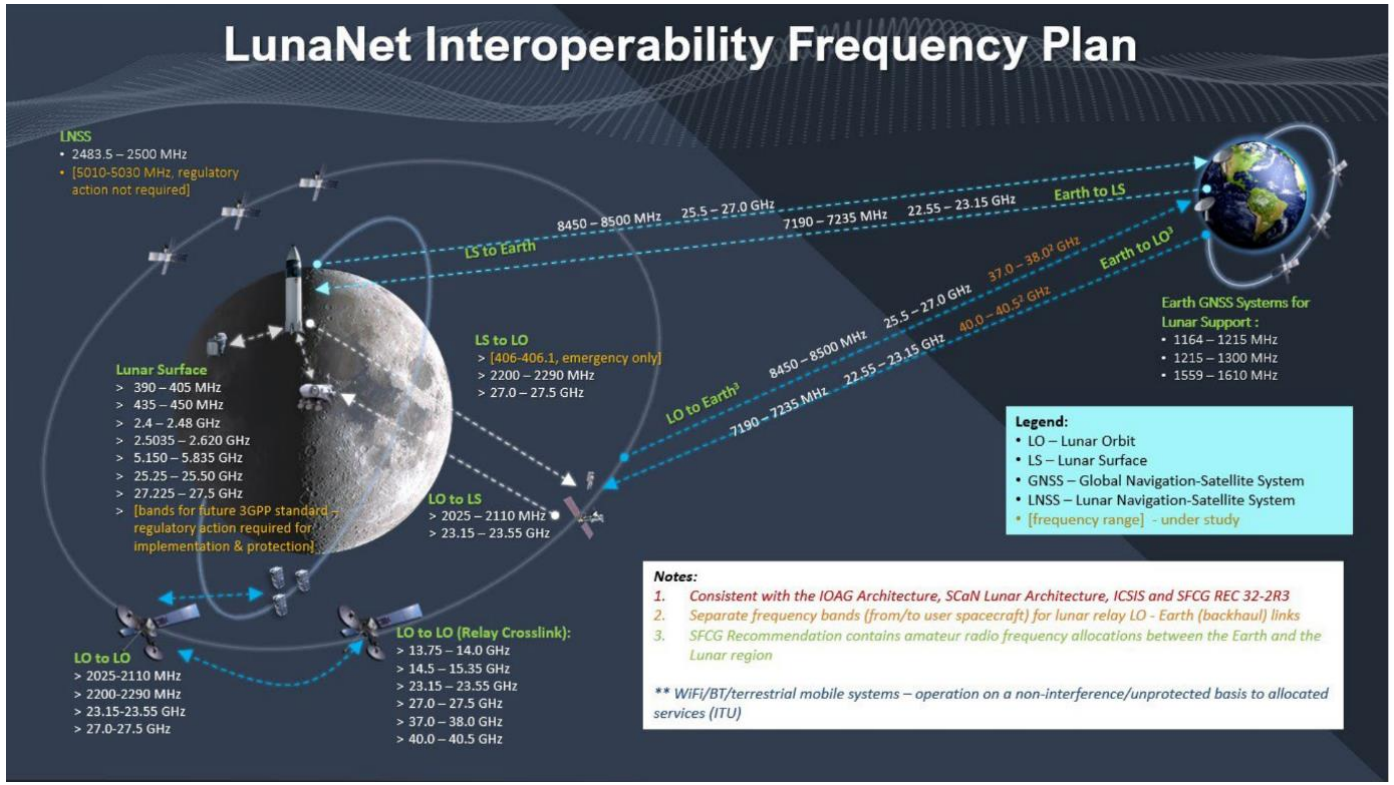

Multiple simulants are accessible, but not all are created with RF in mind.

Methodology

Preliminary Simulant Chemical Composition

Table 1. Chemical composition of a prototype for the lunar highland simulant [3]

Oxide:	SiO_2	Al_2O_3	FeO	MgO	CaO	Na_2O
Weight %	47.6	24.4	4.3	8.5	13.1	1.4

Figure 1: Sample of lunar highlands regolith simulant LHT-2M

Methodology

The dielectric properties of a material, such as its permittivity and loss tangent, affect its RF transmission and reflection. Electrical characteristics of a material are described by the dielectric constant, *K*, permittivity, ε, and conductivity, σ. The dielectric constant is related to the complex permittivity, defined relative to values at vacuum:

$$K = \frac{\varepsilon}{\varepsilon_0} = \varepsilon_r = \varepsilon_r' - j\,\varepsilon_r'' = \frac{\varepsilon_r'}{\varepsilon_0} - j\frac{\sigma}{\omega\varepsilon_0}$$

where the real and imaginary parts of the complex relative permittivity, ε_r are given by ε_r' and ε_r'', respectively. The vacuum permittivity is given by ε_0 and ω is the radial frequency. The loss tangent is defined as the ratio of the energy lost to the energy stored, which is the ratio of the imaginary part of the permittivity to the real part:

$$\tan\delta = \frac{\varepsilon_r''}{\varepsilon_r'}$$

For RF propagation modeling, the real and imaginary parts of the relative permittivity (and therefore the loss tangent) are essential parameters. Dielectric impedance measurement or dielectric spectroscopy is the process of measuring these electrical properties of materials over a range of frequencies.

Methodology

Parameter	Accuracy/Precision
Real Dielectric Permittivity (isolated)	-Range: 1 to 80 where 1 = air, 80 = Distilled Water -Accuracy: < ± 0.5% Or ± 0.25 dielectric units
Imaginary Permittivity	-Range: 0 to 80 -Accuracy: ± 0.1 up to 0.25 S/m and ± 7 at or above 0.5 S/m
Soil Moisture for Inorganic Mineral Soils	-Range: completely dry to Full saturation -Accuracy: ±0.01 WFV for most soils (θ m^3, m^{-3}) ± ≤0.03 for fine textured soils
Bulk Electrical Conductivity	-Accuracy: ±2.0% or 0.02 S/m (whichever is greater) -Range: 0 to 1.5 S/m
Temperature	Accuracy: ±0.3°C Range: -10 to 60°C

50 MHz Time Domain Reflectometry measurement device

Experimental Setup (Temperature measurements)

Temperature sweep from 60°C - 24°C

The simulant was baked at 130 °C for a minimum of 2.5 hours

The testing apparatus was covered in aluminum foil for moisture isolation & performed under a fume hood

Required a thermocouple for accurate time-dependent temperature measurements

Experimental Setup (Moisture measurements)

The simulant was baked at 130 °C for a minimum of 2.5 hours

The testing was performed under a fume hood

Water volume fraction was increased to 40% in roughly 10mL increments

Following the polynomial curve fitting calibration, using the Topp equation [7] (below), a polynomial fit of ε_r' from soil moisture content was calibrated for the sensor. Where θ is the moisture volume fraction:

$$\theta = A + B\varepsilon_r' + C\varepsilon_r'^2 + D\varepsilon_r'^3$$

Results

Measurement results for dry simulant at room temperature

Parameter	Mean	Standard Deviation
Temperature (°C)	23.84	0.089
Soil Moisture (%)	0.16	0.376
Real Permittivity ε_r'	2.75	0.115
Imaginary Permittivity ε_r''	0.13	0.047
Loss Tangent [tan δ]	0.047	0.015

Methodology

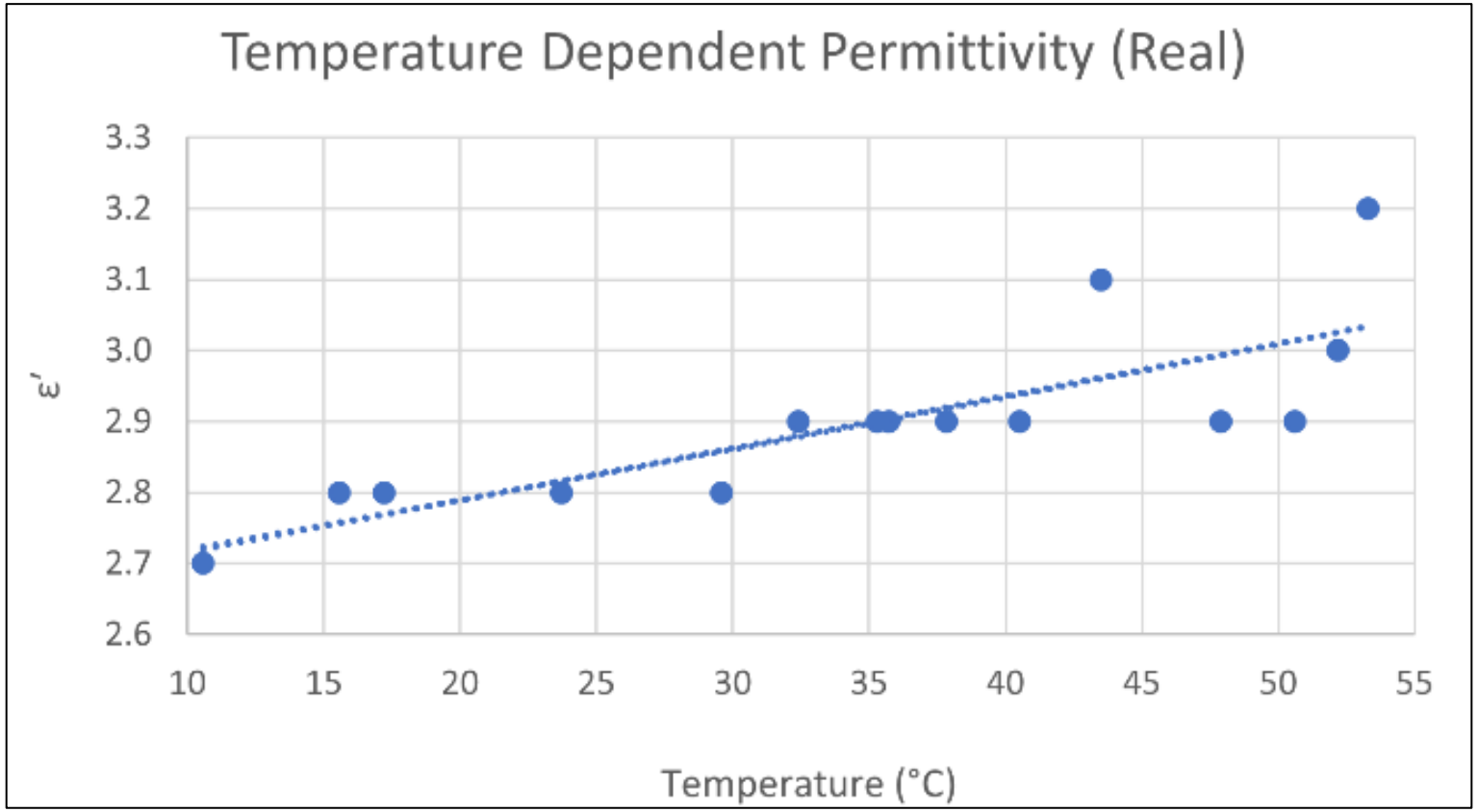

Figure 4: The real permittivity of the simulant as a function of temperature.

Methodology

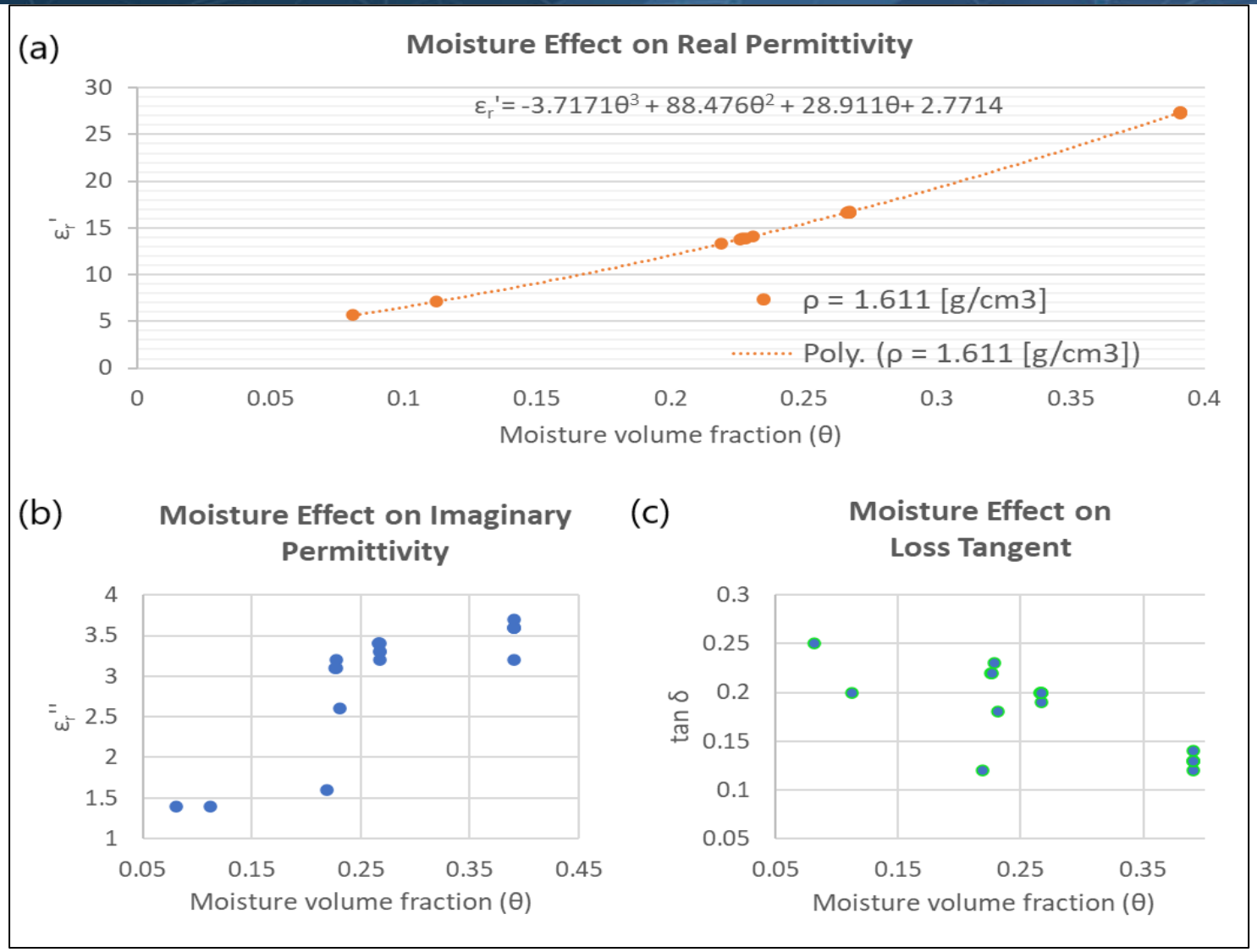

$$\theta = (9 \times 10^{-6})(\varepsilon_r')^3 - 0.0007(\varepsilon_r')^2 + 0.0287\varepsilon_r' - 0.0611$$

Figure 3: Plots of (a) real permittivity, (b) imaginary permittivity, and (c) loss tangent of the simulant as a function of moisture level.

Methodology

The Maxwell Garnett equation is utilized as an approximation for the effective permittivity, εeff, of a given heterogenous medium [8]. The volume fraction contributed by each species in a mixed system influences the effective permittivity in a proportional manner. For the case of the simulant, a multiphase mixture (those that include more than one 'inclusion' constituent with an associated permittivity in a prevailing environmental species with a permittivity of its own), the equation takes the following form if spheroid particles are assumed

$$\varepsilon_{eff} = \varepsilon_e + 3\varepsilon_e \frac{\sum_{k=1}^{k} f_k \frac{\varepsilon_k - \varepsilon_e}{\varepsilon_k + 2\varepsilon_e}}{1 - \sum_{k=1}^{k} f_k \frac{\varepsilon_k - \varepsilon_e}{\varepsilon_k + 2\varepsilon_e}}$$

where εk is the permittivity of the k-th component, f_k is the volume fractional percent and εe is the permittivity of the surrounding medium, which in this case is assumed to be air. The fractional percentage and corresponding permittivity for each of the components in the NU-LHT-2M (NASA/USGS-Lunar Highlands type) simulant is given below

Permittivity of NU-LHT-2M components and corresponding fractional percents

	SiO_2	Al_2O_3	CaO	MgO	FeO	Na_2O
ε_r	3.9 [9]	9-10 [10]	11.95 [11]	9.1-11.2 [12]–[14]	~25 [15], [16]	7.57 [17]
f	47.93	24.57	13.2	8.55	4.33	1.41

Methodology

Ground Penetrating Radar slide placeholder

Table 1: Measurement results for dry simulant at room temperature

Parameter	Mean	Standard Deviation
Temperature (°C)	23.84	0.089
Soil Moisture (%)	0.16	0.376
Real Permittivity ε_r'	2.75	0.115
Imaginary Permittivity ε_r''	0.13	0.047
Loss Tangent [tan δ]	0.047	0.015

Methodology

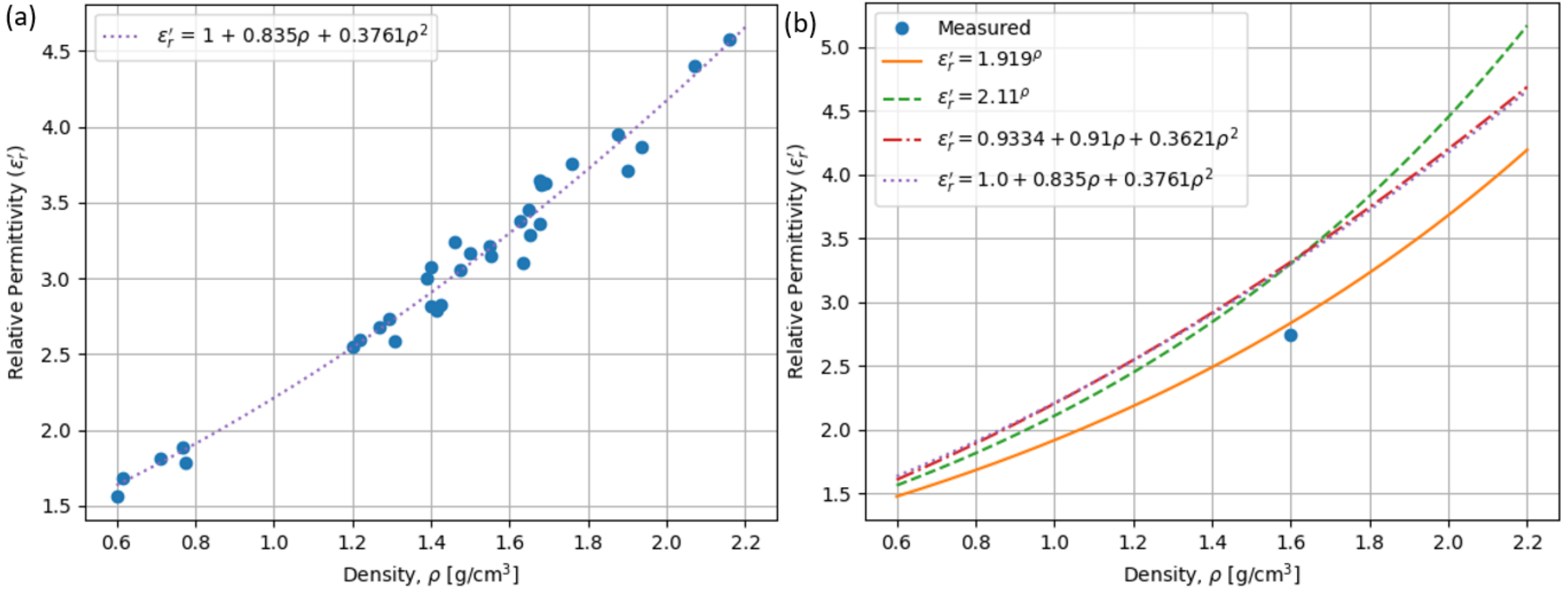

Figure 5: (a) (left) Curve fit to Barmatz 2023 lunar simulant data [22] with curve fit intercept value of one. (b) (right) Relative permittivity models as a function of density. The value of the relative permittivity as measured by the probe in this work is depicted as the "Measured" value.

Methodology

Table 5: Modeled relative permittivity compared to measured value using ρ = 1.598 g/cm^3

	Measurement	Maxwell-Garnett	$\varepsilon_r' = A^\rho$		$\varepsilon_r' = c + b\rho + a\rho^2$	
Parameters	HydraProbe	Table 4	A = 1.919	A = 2.11	c = 0.9334 b = 0.91 a = 0.3621	c = 1.0 b = 0.835 a = 0.3761
Permittivity ε_r'	2.75 std=0.115	2.920	2.833	3.298	3.312	3.295
Modeled Material	NU-LHT-2M	NU-LHT-2M	Apollo Regolith	Multiple Simulants	Multiple Simulants	Multiple Simulants

Concluding Remarks

KPLO image of Tsiolkovskiy Crater

Testing Methods

Current Method:
Waveguide [Ka Band]

Fabrication of Cavity Resonators

Coaxial Probe ε_r		Broadband, convenient, non-destructive; Best for lossy MUTs; liquids and semi-solids
Transmission Line ε_r and μ_r	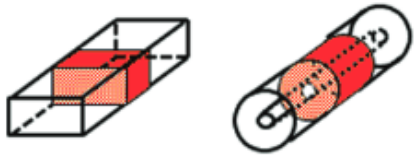	Broadband Best fpr lossy to low loss MUTs; machineable solids
Free Space ε_r and μ_r	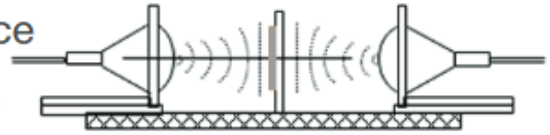	Broadband; Non-contacting Best for flats sheets, powders, high temperatures
Resonant cavity ε_r and μ_r	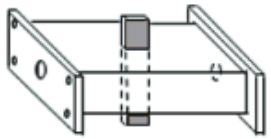	Single frequency; Accurate Best for low loss MUTs; small samples
Parallel plate ε_r	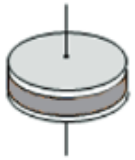	Accurate Best for low frequencies; thin, flat sheets
Inductance measurement μ_r		Accurate, simple measurement, a toroidal core sturcture is required

Transition to Lunar Surface Propagation

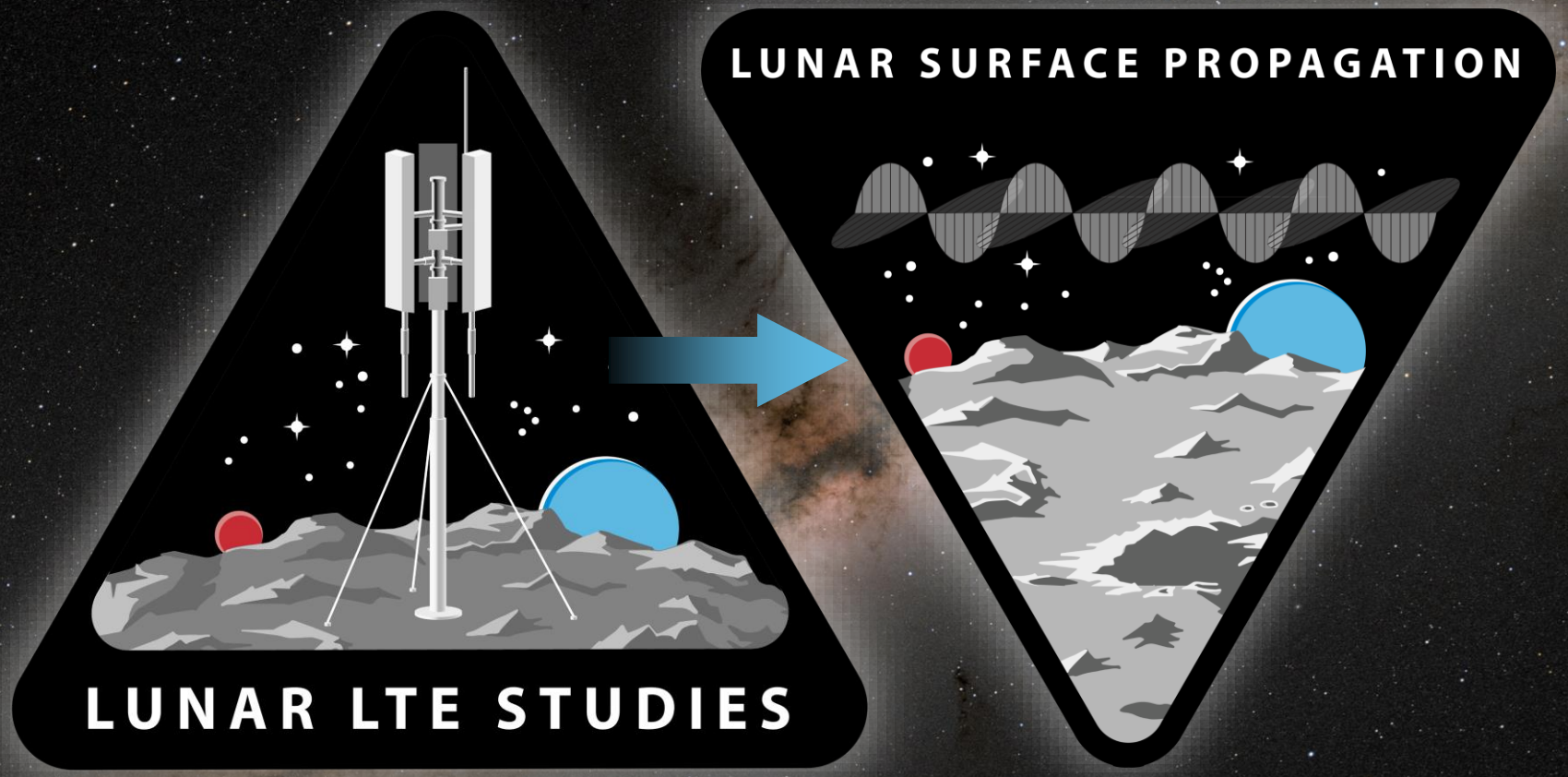

Beginning FY24, LunarLiTES transition into **Lunar Surface Propagation**, capitalizing on the modeling and emulation capabilities developed under LunarLiTES, while expanding beyond the initial IM-2/3GPP focus for relevancy to any Lunar surface RF propagation. Standardization of models and coordination with the international community/ITU will be emphasized.

Citations

[1] V. L. Prabhu, “Microwave heating of lunar simulants JSC-1A and NU-LHT-3M: experimental and theoretical analysis”.
[2] Space Frequency Coordination Group, “Recommendation SFCG 32-2R5: Communication and positioning, navigation, and timing frequency allocations and sharing in the lunar region.” 2023. [Online]. Available: https://www.sfcgonline.org/Resources/Recommendations/default.aspx
[3] D. Stoeser, D. Rickman, and S. Wilson, “Design and Specifications for the Highland Regolith Prototype Simulants NU-LHT-1M and -2M,” 2010. Accessed: Sep. 20, 2023. [Online]. Available: https://www.semanticscholar.org/paper/Design-and-Specifications-for-the-Highland-Regolith-Stoeser-Rickman/5d64100053c55e44a79734d167e9d6393963d8a9
[4] X. Zeng, C. He, and A. Wilkinson, “Geotechnical Properties of NT-LHT-2M Lunar Highland Simulant,” *J. Aerosp. Eng.*, vol. 23, no. 4, pp. 213–218, Oct. 2010, doi: 10.1061/(ASCE)AS.1943-5525.0000026.
[5] Stevens, “Hydroprobe Manuel.” 2018. [Online]. Available: https://stevenswater.com/resources/documentation/hydraprobe/HydraProbe_Manual_Jan_2018.pdf
[6] “What is a type K Thermocouple?,” *https://www.omega.com/en-us/*. https://www.omega.com/en-us/resources/k-type-thermocouples (accessed Sep. 19, 2023).
[7] G. C. Topp, J. L. Davis, and A. P. Annan, “Electromagnetic determination of soil water content: Measurements in coaxial transmission lines,” *Water Resour. Res.*, vol. 16, no. 3, pp. 574–582, 1980, doi: 10.1029/WR016i003p00574.
[8] A. Sihvola, *Electromagnetic Mixing Formulas and Applications*. IET Digital Library, 1999. doi: 10.1049/PBEW047E.
[9] P. Zukowski, T. N. Koltunowicz, K. Czarnacka, A. K. Fedotov, and I. E. Tyschenko, “Carrier transport and dielectric permittivity of SiO2 films containing ion-beam synthesized InSb nanocrystals,” *J. Alloys Compd.*, vol. 846, p. 156482, Dec. 2020, doi: 10.1016/j.jallcom.2020.156482.
[10] S. J. Penn *et al.*, “Effect of Porosity and Grain Size on the Microwave Dielectric Properties of Sintered Alumina,” *J. Am. Ceram. Soc.*, vol. 80, no. 7, pp. 1885–1888, Jan. 2005, doi: 10.1111/j.1151-2916.1997.tb03066.x.
[11] M. A. Subramanian, R. D. Shannon, B. H. T. Chai, M. M. Abraham, and M. C. Wintersgill, “Dielectric constants of BeO, MgO, and CaO using the two-terminal method,” *Phys. Chem. Miner.*, vol. 16, no. 8, pp. 741–746, Nov. 1989, doi: 10.1007/BF00209695.
[12] H. Kassem *et al.*, “LaTiOxNy Thin Films, Measurement and Application to Microwave Device,” *2008 38th Eur. Microw. Conf.*, pp. 1362–1365, Oct. 2008, doi: 10.1109/EUMC.2008.4751717.
[13] J. D. Hwang and C.-Y. Chang, “Post-annealing treatment in improving high dielectric constant MgO-based metal-oxide-semiconductor diodes,” *Appl. Phys. Lett.*, vol. 120, no. 25, p. 252902, Jun. 2022, doi: 10.1063/5.0094513.
[14] S. Lee *et al.*, “Enhanced dielectric properties of Be-doped magnesium oxide nanopowder,” *AIP Adv.*, vol. 13, no. 1, p. 015007, Jan. 2023, doi: 10.1063/5.0130595.
[15] *Non-Tetrahedrally Bonded Binary Compounds II*. Accessed: Sep. 20, 2023. [Online]. Available: https://link.springer.com/book/9783540649663
[16] L.-S. Fu, J.-T. Jiang, C.-Y. Xu, and L. Zhen, “Synthesis of hexagonal Fe microflakes with excellent microwave absorption performance,” *CrystEngComm*, vol. 14, no. 20, pp. 6827–6832, Sep. 2012, doi: 10.1039/C2CE25836F.
[17] I. Petousis *et al.*, “High-throughput screening of inorganic compounds for the discovery of novel dielectric and optical materials,” *Sci. Data*, vol. 4, no. 1, Art. no. 1, Jan. 2017, doi: 10.1038/sdata.2016.134.
[18] G. R. Olhoeft and D. W. Strangway, “Dielectric properties of the first 100 meters of the Moon,” *Earth Planet. Sci. Lett.*, vol. 24, no. 3, pp. 394–404, Jan. 1975, doi: 10.1016/0012-821X(75)90146-6.
[19] W. D. Carrier III, G. R. Olhoeft, and W. Mendell, *Physical Properties of the Lunar Surface*. 1991, pp. 475–594. Accessed: Sep. 20, 2023. [Online]. Available: https://ui.adsabs.harvard.edu/abs/1991lsug.book..475C
[20] J. Lai, Y. Xu, X. Zhang, and Z. Tang, “Structural analysis of lunar subsurface with Chang′E-3 lunar penetrating radar,” *Planet. Space Sci.*, vol. 120, pp. 96–102, Jan. 2016, doi: 10.1016/j.pss.2015.10.014.
[21] J. Feng, Y. Su, C. Ding, S. Xing, S. Dai, and Y. Zou, “Dielectric properties estimation of the lunar regolith at CE-3 landing site using lunar penetrating radar data,” *Icarus*, vol. 284, pp. 424–430, Mar. 2017, doi: 10.1016/j.icarus.2016.12.005.
[22] M. Barmatz, D. Steinfeld, J. Batres, H.-Y. Hao, D. Rickman, and H. Shulman, “Microwave permittivity and permeability measurements on lunar simulants at low temperatures,” *Adv. Space Res.*, Aug. 2023, doi: 10.1016/j.asr.2023.08.041.
[23] M. A. Siegler, J. Feng, P. G. Lucey, R. R. Ghent, P. O. Hayne, and M. N. White, “Lunar Titanium and Frequency-Dependent Microwave Loss Tangent as Constrained by the Chang’E-2 MRM and LRO Diviner Lunar Radiometers,” *J. Geophys. Res. Planets*, vol. 125, no. 9, p. e2020JE006405, 2020, doi: 10.1029/2020JE006405.